Ocean Engineering 306 (2024) 118064

Contents lists available at ScienceDirect

Ocean Engineering

journal homepage: www.elsevier.com/locate/oceaneng

Comparison study of the vortical structures in the wake of a rim-driven thruster and a ducted propeller in bollard conditions

Bao Liu [a,b], Xinping Yan [a,b,c,d], Wu Ouyang [a,b,c,d,*], Maarten Vanierschot [e,f]

[a] School of Transportation and Logistics Engineering, Wuhan University of Technology, Wuhan 430063, China
[b] State Key Laboratory of Maritime Technology and Safety, Wuhan University of Technology, Wuhan 430063, China
[c] Reliability Engineering Institute, National Engineering Research Center for Water Transport Safety, Wuhan 430063, China
[d] East Lake Laboratory, Wuhan 420202, China
[e] KU Leuven, Department of Mechanical Engineering, Leuven 3001, Belgium
[f] North-West University, Material Science, Innovation and Modelling (MaSIM) Research Focus Area, Mmabatho 2745, South Africa

ARTICLE INFO

Keywords:
Vortical structures
Rim-driven thruster
Proper orthogonal decomposition
Noise performance

ABSTRACT

This paper studies the vortical structures found in the wake of a ducted propeller (DP) and a rim-driven thruster (RDT) in bollard conditions. Despite a good understanding of the vortical structures in the wake of DPs, an understanding of these structures and their dynamics in the wake of RDTs is largely lacking. At bollard conditions, noise levels are higher compared to other loading conditions due to the higher pressure fluctuations in the wake. Hence, understanding the flow structures in the wake is a necessity to understand the noise production and propagation. Both wake flows were analysed using visualization of the instantaneous vortical structures, frequency spectra at several locations in the flow field and proper orthogonal decomposition (POD). It was shown that the centre of the wake in both the DP and RDT contained several spiralling structures behind the central hub. These structures contained a wide range of frequencies, making the wake very dynamic with a broad range of different coherent fluctuations. In case of the RDT, these structures persisted longer in the flow field before breaking up into smaller turbulent structures. In the DP wake, very strong tip vortices were formed in the gap flow between the duct and the propeller blades, which were not present in the RDT. These tip vortices interacted with the flow around the duct to form a shear layer with large pressure fluctuations. As these tip vortices induce higher sound levels, the RDT shows a significantly better noise performance compared to the DP.

1. Introduction

Noise problems in marine propellers have become an important criterion in the evaluation of the propeller's overall performance. It is necessary to make sure that the propeller can maintain a sufficient hydrodynamic efficiency while keeping a reduced radiated noise level in many situations. Sometimes the elimination of noise has an even higher priority than the hydrodynamic efficiency, for instance in submarines, where the capabilities of invisibility highly depend on the sound level emitted. For underwater vehicles, reduction of noise can also facilitate the implementation of tasks as well as reduce harms to marine wildlife (Yu et al., 2020). Currently in many cases, the noise caused by the propeller's motion has become one of the most significant sources of noise for marine vessels or underwater vehicles (Wang et al., 2018). When fluid passes through the propeller, the interactions between the flow and propeller induce noise and vibrations caused by the unsteadiness of the flow field, which is related to the propeller geometry and load (Viitanen et al., 2018). The flow field is very complex and distinct vortical structures are generated on the blade surface and they are convected downstream in non-linear patterns. These coherent structures can often maintain their structure and shape for a certain period until instabilities occur, resulting in their break-up in the far field. During the evolution of the wake vortical system, vortices shed from different parts of the propeller often exhibit strong self- and mutual induction, causing these instabilities and associated break-up (Gong et al., 2018). The instability mode is related to the helical pitch, the vortex core size and the vortex strength. Since the dynamic development of the wake vortices is highly responsible for the oscillations and noise performance of the propeller, it is considered to be paramount to have a thorough understanding of the flow mechanisms as they can often provide valuable insights into improved hydrodynamic performance prediction and optimization design (Baek et al., 2015).

* Correspondence to: Heping Road No. 1178, Wuchang District, Wuhan City, Hubei Province, China.
E-mail address: ouyangw@whut.edu.cn (W. Ouyang).

https://doi.org/10.1016/j.oceaneng.2024.118064
Received 27 February 2024; Received in revised form 28 April 2024; Accepted 28 April 2024
Available online 14 May 2024

A visualization of the propeller wake composition and evolution can be performed using experimental methods. In order to figure out the evolution mechanisms of the tip and hub vortices of a marine propeller in the transition and far field, Felli et al. (2011) took advantage of modern visualization tools, such as high speed cameras and Laser Doppler Velocimetry (LDV), to capture the instantaneous flow fields for analysis. The wake evolution of a propeller operating in oblique flows was investigated using Particle Image Velocimetry (PIV) measurements in Felli and Falchi (2018). It was found that changing the oblique angle of the inflow significantly influenced the vortical structures of the propeller, such as the morphology and interaction mechanisms of the wake vortical system.

The costs in setting up a test platform can be quite high and experimental measurements of flow quantities can be very difficult. In recent years, numerical simulations are gaining more popularity as they can provide even more detailed information about the flow field with less costs if used properly. For example, Baek et al. (2015) studied the wake evolution of an open propeller under different advance coefficients by solving the unsteady 3-D incompressible Navier–Stokes equations with the SST k–ω turbulence model, and they found that the wake topology is more distinct at low advance coefficients compared to high advance coefficients. Wang et al. (2018) numerically studied the influence of the skew angle on the propeller's trailing vortex. An improved detached eddy simulation was employed by Wang et al. (2021, 2023) to study the wake instability mechanisms of a marine propeller. Jiang et al. (2021) compared different turbulence models on the prediction of propeller wake fields.

Apart from studies of propellers in normal open water conditions, wake dynamics are also investigated under some special scenarios. Viitanen et al. (2018) employed delayed detached eddy simulations (DDES) to study the hydroacoustics of the Potsdam propeller test case (PPTC) in both wetted and cavitating conditions. Lungu (2020) numerically investigated the hydrodynamic performance of a controllable pitch propeller developed by Potsdam Basin using the detached eddy simulation method under both cavitating and non-cavitating conditions. Wang et al. (2019) explored the wake dynamics of a propeller and rudder interaction with detached eddy simulations. Different advance coefficients and rudder angles were considered and it was shown that under heavy load conditions, the topology of the vortex system becomes more complex and the interaction between the wake and the rudder is stronger. In another work of Lungu (2022), the interactions of propeller and hull of an underwater vehicle were studied. Different working conditions were considered, including a deep immersion and free surface scenario with various depths. Posa et al. (2023) investigated the acoustic characteristics of a propeller working in the wake of a hydrofoil.

It is often observed that the wake vortices exhibit different patterns based on propeller loading conditions and geometrical profiles. For open propellers, the development of the wake vortical structures is mainly affected by the mutual interactions of vortex shedding from adjacent blades. However, for a ducted propeller (DP), the existence of the duct complicates the composition and evolutionary mechanism of these wake vortices. Tip leakage vortices are formed due to the tip clearance between the blade tip and the duct's interior surface. At the trailing edge of the duct, flow separates from the duct and interacts with the propeller tip vortices, causing different wake evolution patterns compared to an open propeller. Gong et al. (2018) made a comparison study of wake dynamics between open and ducted propellers using detached eddy simulations (DES). In the research of Guo et al. (2023), jet flow is introduced to improve the hydrodynamic performance of a ducted propeller. Zhang and Jaiman (2019) investigated the wake dynamics of a DP by employing delayed detached eddy simulations (DDES) along with the sliding mesh approach and concluded that the bollard condition triggers the most complex wake flow patterns regarding turbulence distribution among all the simulated cases. Gong et al. (2021) investigated the hydrodynamic loads and wake dynamics of a DP operating in oblique flows using the detached eddy simulation approach. Zhang et al. (2022) adopted the improved delayed detached eddy simulation method to capture the tip leakage vortex with different tip clearance dimensions. Zhu and Gao (2019) used a large eddy simulation model to simulate the tip vortex cavitation of a propeller with winglets. Zhao et al. (2023) made a comparison study of the wake dynamics of a pump-jet propulsor and a ducted propeller. Bionic structures were employed in Yang et al. (2024) to improve the noise performance of a ducted propeller.

A rim-driven thruster (RDT), which integrates the propeller and motor, also consists of a duct and a propeller (Yan et al., 2017) and therefore can be regarded as a special kind of DP. However, unlike a DP, there is no tip clearance and therefore no tip leakage vortices are present. Instead, there is another important flow feature present in an RDT, i.e. the gap flow, which is characterized by a channel of small dimensions and exhibits significant influence on the overall performance of the thruster, particularly at model scale. In terms of hydrodynamic analyses, current studies on RDTs are mainly focused on numerical modelling (Dubas et al., 2015; Liu et al., 2022a; Li et al., 2023a,b) and general hydrodynamic performance prediction (Yakovlev et al., 2011; Song et al., 2015; Liu and Vanierschot, 2021; Liu et al., 2023c,b). There are also several researches on the optimization design of RDTs focused on single components such as duct or propeller. Gaggero (2020) developed a simulation-based optimization design framework for the optimization design of propellers. Zhai et al. (2022) employed a parametric method to define the duct profile and finally, a gain of 3.3% in efficiency was realized. In the work of Liu et al. (2023b), the adjoint approach was utilized to optimize the profile of an RDT duct. A multi-parameter collaborative optimization framework is proposed by Nie et al. (2023) to improve the efficiency of RDTs based on the response surface method.

In contrast to ducted propellers, numerical studies on the details of the vortical structures in the wake of an RDT are much more scarce. Moreover, despite the importance of the vortical structures on the noise emitted by propellers, to the authors' knowledge, a detailed comparison between a DP and RDT is currently missing. Even though in the research of Witte et al. (2019), the unsteady wake of a hubless propeller at bollard condition was investigated, the rim gap was not modelled in the simulation. Nevertheless, considering the huge influence of geometry and structure on the generation of these vortical structures, the gap formed by the rim and duct interior surface is liable to affect the formation of propeller tip vortices. Therefore it is meaningful to conduct a study on the comparison of wake composition and evolution between a DP and an RDT in order to better understand the influence of the structural difference on the performance of the propeller and the mechanisms behind, as both are crucial for the improvement of performance prediction and optimization design. Therefore, this study aims to extend the knowledge on the wake structure and dynamics of an RDT compared to a DP in bollard conditions. At bollard conditions, noise levels are higher compared to other loading conditions due to the higher pressure fluctuations in the wake. The rest of the paper is organized as follows. The model set-up and its validation are described in Section 2, followed by the analysis of wake fields of the DP and RDT in Section 3, including the hydrodynamic characteristics and several important flow features and finally some conclusions are drawn based on the results in Section 4.

2. Theoretical background

2.1. Governing equations

The ensemble averaged or filtered governing equations for incompressible Newtonian turbulent fluid flows are given in tensor notation as:

$$\frac{\partial \overline{U}_i}{\partial x_i} = 0, \tag{1}$$

$$\frac{\partial \overline{U}_i}{\partial t} + \overline{U}_j \frac{\partial \overline{U}_i}{\partial x_j} = -\frac{1}{\rho}\frac{\partial \overline{p}}{\partial x_i} + \nu \frac{\partial^2 \overline{U}_i}{\partial x_j \partial x_j} - \frac{\partial \tau_{ij}}{\partial x_j}, \tag{2}$$

where ρ is the fluid density, $\overline{U}_i$ (i, j = 1, 2, 3) is the ensemble averaged or filtered velocity component, t is the flow time, p is the pressure, ν is the kinematic viscosity, and τ_{ij} is the residual stress tensor. In this study, turbulence is modelled using the Delayed Detached Eddy Simulation (DDES) approach as this model gives very good predictions for DP flows (Viitanen et al., 2018; Zhang and Jaiman, 2019). DDES employs the Reynolds Averaged Navier–Stokes (RANS) approach (where the overline symbol represents ensemble averaged quantities in Eqs. (1) and (2)) in the boundary layer, while LES is used in the free stream and for the LES part, the overline symbol represents filtered quantities. For the RANS part of the flow, an SST $k-\omega$ model (Menter, 1994) is used and the residual stress τ_{ij} is given as

$$\tau_{ij} = \overline{u_i' u_j'} = -\nu_t \left(\frac{\partial \overline{U}_i}{\partial x_j} + \frac{\partial \overline{U}_j}{\partial x_i} \right) + \frac{2}{3} k \delta_{ij}, \tag{3}$$

where ν_t is the turbulent viscosity, k the turbulent kinetic energy and δ_{ij} is the Kronecker symbol. For the LES part of the flow, the residual stress tensor is given as

$$\tau_{ij} = \overline{U_i U_j} - \overline{U}_i \overline{U}_j - \frac{2}{3} k_r \delta_{ij}, \tag{4}$$

where $k_r = 0.5(\overline{U_i U_j} - \overline{U}_i \overline{U}_j.)$. In the LES part of the domain, the dynamic Smagorinsky–Lilly model is used as turbulence closure. Since the subgrid-scale stresses resulting from the filtering operation are unknown, and require modelling, the subgrid-scale turbulence models in ANSYS FLUENT employ the Boussinesq hypothesis to compute the subgrid-scale turbulent stresses. In the Smagorinsky–Lilly model, the eddy viscosity μ_t is calculated from

$$\mu_t = \rho L_s^2 \left| \overline{S} \right|, \tag{5}$$

where $\left| \overline{S} \right| = \sqrt{2 \overline{S}_{ij} \overline{S}_{ij}}$ and L_s is the mixing length for the subgrid scale, determined by

$$L_s = min(\kappa d, C_s \Delta), \tag{6}$$

where κ is the von Karman constant, d is the distance to the closest wall, C_s is the Smagorinsky constant, and Δ is the local grid scale and is calculated based on the volume the grid cell using

$$\Delta = V^{1/3}. \tag{7}$$

In ANSYS Fluent, the default value of C_s is 0.1. However, in the dynamic Smagorinsky–Lilly model, the Smagorinsky constant is no longer given in advance but computed based on the resolved flow field.

2.2. Reduced order modelling

In research on turbulence, the Reynolds decomposition is widely used to extract stochastic fluctuations of a specific physical quantity. However, this approach is not suitable for turbulent flows sustaining a well-organized large-scale coherent motion, like the rotation of the propeller blades of a DP or RDT. To separate the fluctuations induced by this rotation from turbulence, the flow field is decomposed using proper orthogonal decomposition (POD). The flow field $\boldsymbol{u}(\boldsymbol{x}, t) = (u, v, w)$ is decomposed into a time averaged and fluctuation part as:

$$\boldsymbol{u}(\boldsymbol{x}, t) = \langle \boldsymbol{u}(\boldsymbol{x}, t) \rangle + \boldsymbol{u}^{\dagger}(\boldsymbol{x}, t), \tag{8}$$

where $\langle \boldsymbol{u}(\boldsymbol{x}, t) \rangle$ is the time-averaged value and $\boldsymbol{u}^{\dagger}(\boldsymbol{x}, t)$ is the fluctuation part. Taking N time series data collected from M grid points in a three-dimensional volume with $N \ll M$ into account, the fluctuating part in Eq. (8) is split into a collection of spatial modes:

$$\boldsymbol{u}(\boldsymbol{x}, t) = \langle \boldsymbol{u}(\boldsymbol{x}, t) \rangle + \boldsymbol{u}^{\dagger}(\boldsymbol{x}, t) = \langle \boldsymbol{u}(\boldsymbol{x}, t) \rangle + \sum_{i=1}^{N} a_i(t) \boldsymbol{\Phi}_i(\boldsymbol{x}). \tag{9}$$

Here, $\boldsymbol{\Phi}_i(\boldsymbol{x})$ represents a spatial POD mode and $a_i(t)$ is the corresponding temporal coefficient. The temporal coefficient $\boldsymbol{a}_i = [a_i(t_1), a_i(t_2), \ldots, a_i(t_N)]^T$ and mode energies λ_i are obtained from the eigenvectors and eigenvalues of matrix $\boldsymbol{R}$:

$$\boldsymbol{R}\boldsymbol{a}_i = \lambda_i \boldsymbol{a}_i, \quad \lambda_1 \geqslant \lambda_2 \geqslant \cdots \geqslant \lambda_n \geqslant 0, \tag{10}$$

where the correlation matrix $\boldsymbol{R}$ (with a size of $N \times N$) is calculated as

$$R_{i,j} = \frac{1}{N} [\boldsymbol{u}^{\dagger}(\boldsymbol{x}, t_i)]^T [\boldsymbol{u}^{\dagger}(\boldsymbol{x}, t_j)]. \tag{11}$$

Then, the spatial modes $\boldsymbol{\Phi}_i(\boldsymbol{x})$ are calculated by projection of the snapshots onto the temporal coefficients:

$$\boldsymbol{\Phi}_i(\boldsymbol{x}) = \frac{1}{N \lambda_i} \sum_{j=1}^{N} a_i(t_j) \boldsymbol{u}^{\dagger}(\boldsymbol{x}, t_j). \tag{12}$$

2.3. Geometrical model and grid generation

The geometrical models used in this study are presented in Fig. 1 and both the DP and RDT have a uniform gap dimension of 0.6 mm. The computational domain is a cylinder with a length of 10D and a radius of 4D, where D = 0.1m is the diameter of the propeller (as shown in Fig. 2). In a Cartesian coordinate system, the axial direction is the z-axis. The velocity inlet is located 2D upstream of the propeller and the pressure outlet is situated 8D downstream. This setting was observed to avoid confinement effects while not influencing the evolution of the wake flow (Mahesh et al., 2015; Gong et al., 2018; Gaggero, 2023). In order to simulate bollard conditions, a very low velocity value of 0.01 m/s is imposed on the inlet with random turbulent fluctuations having 5% turbulence intensity. At the pressure outlet, Neumann boundary conditions are applied. The side wall of the domain is a symmetry boundary condition. The computational domain consists of a static zone and a rotating zone containing the propeller, rim and hub. To simulate the rotational movement of the propeller, the sliding mesh (SM) approach is employed, as this method has proven to capture the wake structures better than for instance the Moving Reference Frame (MRF) approach (Liu et al., 2022b). The rotational rate of this rotating zone is n, equal to 20 revolutions per second.

In order to improve the accuracy of the numerical results, fully structured meshes are employed for both the RDT and DP. Details of these meshes are shown in Figs. 3 and 4. As the turbulent viscosity in LES depends on the mesh size, an estimation of the discretization error was performed using the RANS model in the entire flow domain. Three sets of meshes have been generated to perform a grid sensitivity study. To quantify the grid error, the results calculated from the different meshes are provided in Table 1. As can be seen, the convergence is non-monotonic and the results of the three different meshes are within 2.2% of each other and very close to the experimental results (K_T = 0.259 and $10K_Q$=0.441 Oosterveld, 1970). Nevertheless, for the LES simulations, the fine mesh is taken to ensure sufficient small cell sizes in the wake. As such, in the LES part of the domain, at least 85% of the turbulent kinetic energy is resolved, which means the LES simulation is well resolved. Second-order central differencing schemes are used for the discretization of the momentum equation, while a second order upwind scheme is used for the turbulence equations. The SIMPLEC algorithm is adopted for the pressure and velocity coupling. For the temporal discretization, a second order scheme is used and the timestep, $t = 1\times10^{-5}$, is chosen to have a maximum Courant number in the order of 1 and an average Courant number of 0.08 in the rotating domain. The y^+ distributions on the surfaces of the DP and RDT are presented in Fig. 5. It needs to be noted that y^+ values on the suction side of the propellers are notably smaller than those on the pressure side and therefore only the former ones are shown. Since the SST $k-\omega$ model was employed to model the flow near the wall and simulating the entire boundary layer accurately up to $y^+ = 1$ is not necessary to study the large scale wake structures, the y^+ values are considered to be within acceptable range.

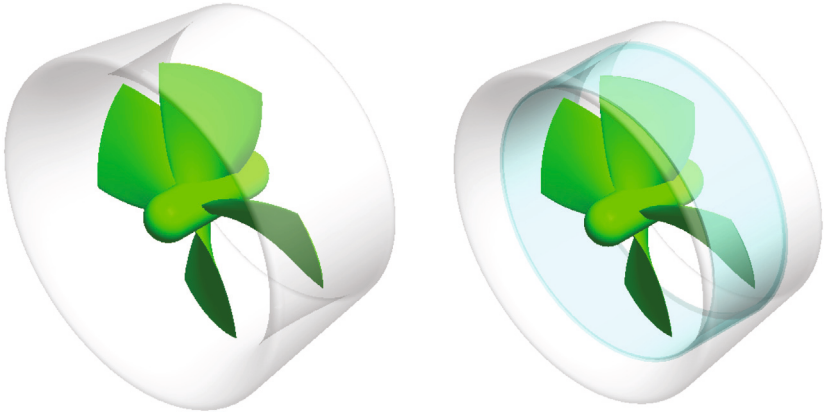

(a) (b)

Fig. 1. Different propellers used in this study: (a) the ducted propeller (DP) and (b) the rim-driven thruster (RDT).

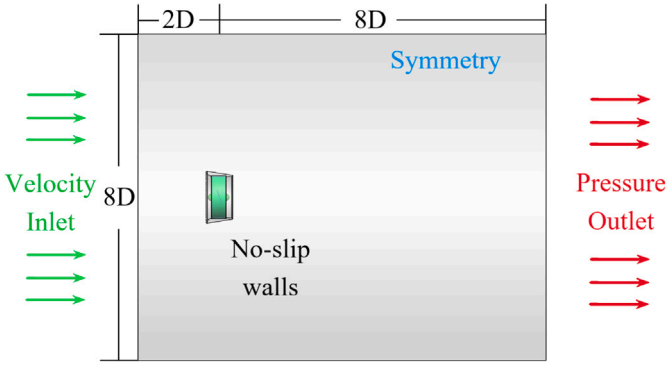

Fig. 2. The computational domain and boundary conditions.

Table 1
Discretization error estimation for the ducted propeller.

Mesh density	Cell counts (million)	Refinement ratio	K_T	$10K_Q$
Coarse	3.5	–	0.260	0.455
Medium	9.5	1.4	0.259	0.454
Fine	24.5	1.4	0.265	0.460

3. Results and discussion

3.1. Time averaged flow fields and statistics

Fig. 6 shows the time averaged axial velocity profiles at various location in the wake behind the DP and the RDT. The profiles are scaled with the representative velocity nD of the propeller, which is 2 m/s in this case ($n = 20$ revolutions per second). Both profiles exhibit a wake-like structure and are very similar to each other, with some subtle differences. Two shear layers can be found, one inner between the central wake and the main flow and one outer between the main flow and the surroundings. The inner shear layer is very thin and near the hub, the velocity deficit in the wake of the DP is more pronounced compared to the one of the RDT (Fig. 6(a)). This velocity deficit is caused by a positive pressure gradient ($\partial p/\partial z > 0$) in the axial direction due to the decrease of rotational velocity downstream. Moving in the downstream direction, the wake recovers faster for the DP compared to the RDT. Unlike the inner shear layer, the outer one between the main flow and surroundings is very similar for both the RDT and DP.

The scaled circumferential velocity profiles are shown in Fig. 7. These profiles show a very fast rotating vortex core with a very small radius, which is the hub wake vortex. This hub vortex rotates slightly faster in the RDT wake compared to the DP, especially further downstream. Near the trailing edge of the duct ($y/R = \pm 1$), the influence of the tip vortices behind the blades of the DP is clear as they make the shear layer behind the duct rotate less fast compared to the RDT (Fig. 7(a)), while having a very small influence on the axial velocity profile. Comparing with Figure Fig. 7(b) also shows that the influence of the tip vortices decreases quite fast downstream as the velocity profiles in the outer shear layer are very similar from $z/R = 2$ on.

In order to better understand the wake evolution, the normalized pressure coefficient C_p is shown in Fig. 8. C_p is defined as

$$C_p = \frac{p - p_\infty}{\frac{1}{2}\rho(nD)^2}, \tag{13}$$

where p is the local static pressure and p_∞ is the pressure in the free-stream. The static pressure in the centre is very low due to the balance between radial pressure gradients and the centrifugal force as

$$\frac{\partial p}{\partial r} = \rho\frac{U_c^2}{r}. \tag{14}$$

Similar to the axial velocity in Fig. 6, the pressure coefficient near the hub is smaller for the DP. Fig. 8 illustrates that the radius of the wake is very small and that the wake recovery of the DP is larger than the RDT, which could also be seen from the axial and circumferential velocity profiles.

A comparison of the root mean square pressure coefficient, which reflects positions where the highest pressure fluctuations occur, is presented in Fig. 9. It can be observed that the general pattern is quite similar, with the major fluctuations concentrated in the hub and tip regions where the vortices are the strongest. Especially just behind the hub, the pressure fluctuations are very strong. The primary difference between the DP and RDT is located at the tip region: the tip leakage flow induced by the tip clearance in the DP intensifies the interactions between the blade tip and duct inner surface, resulting in higher pressure fluctuations.

The resolved turbulent kinetic energy is shown in Fig. 10. The profile is very similar to the one of the pressure coefficient, with the largest values behind the central hub. Due to the tip vortices, the shear layer behind the duct is larder for the DP and it merges earlier with the central hub vortex compared to the RDT.

3.2. Instantaneous flow fields and velocity spectra

The instantaneous vortical structures in the wake field of the DP and RDT, in which the 3D vortical structures are visualized using the velocity magnitude and Q-criterion (Jeong and Hussain, 1995), are

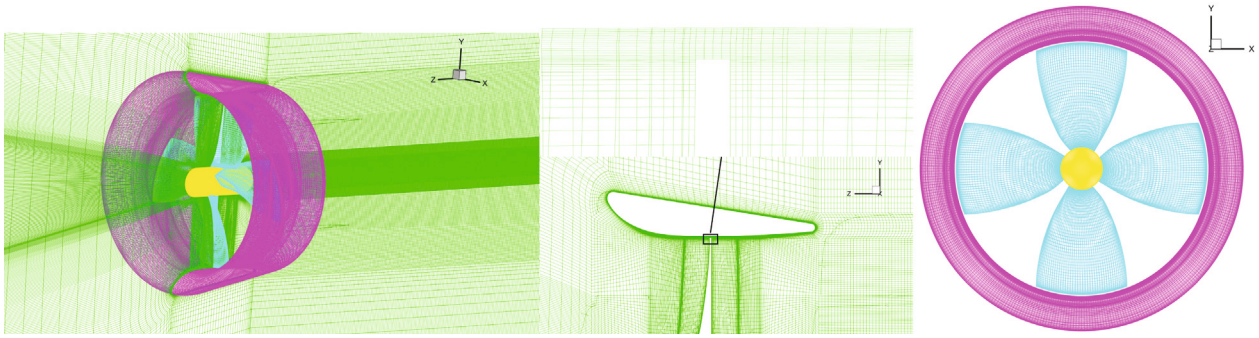

(a) (b) (c)

Fig. 3. The grid discretization for the ducted propeller: (a) Overall mesh distribution, (b) Volume mesh around the propeller and (c) Surface mesh.

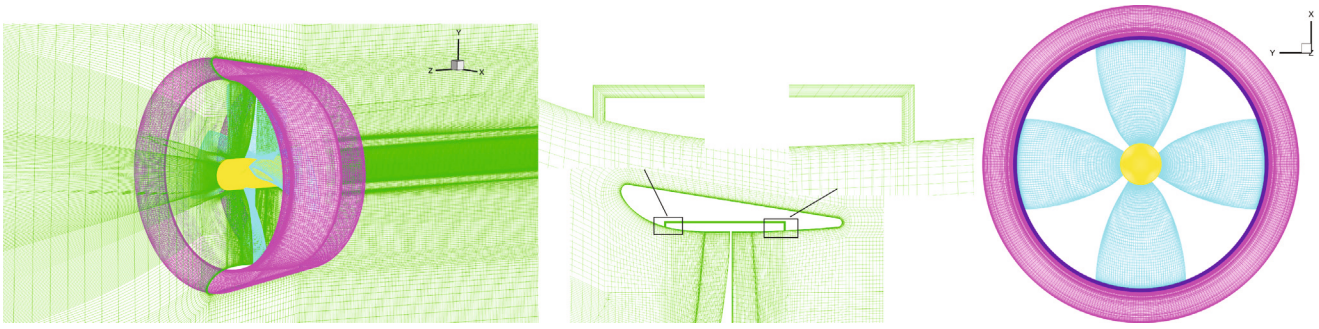

(a) Overall mesh distribution. (b) Volume mesh around the propeller. (c) Surface mesh.

Fig. 4. The grid discretization for the rim-driven thruster: (a) Overall mesh distribution, (b) Volume mesh around the propeller and (c) Surface mesh.

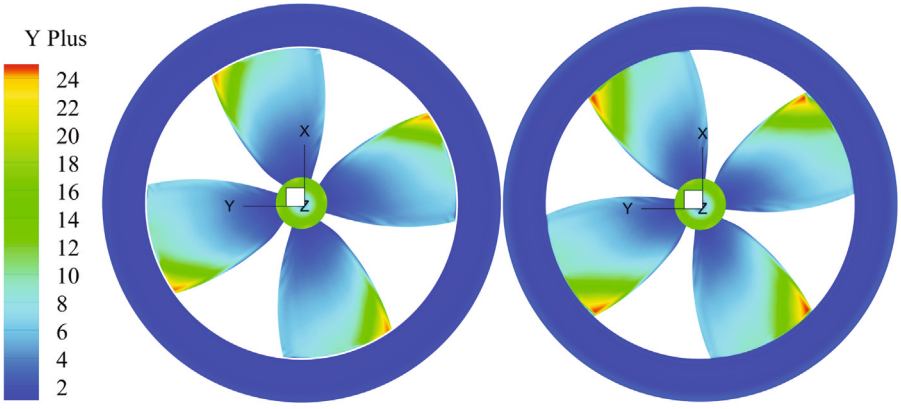

(a) y^+ distribution over the DP. (b) y^+ distribution over the RDT.

Fig. 5. The y^+ distributions over the surfaces of: (a) DP, and (b) RDT.

shown in Fig. 11. In this method, Q is defined based on the velocity gradient tensor $\nabla\overline{\mathbf{U}}$,

$$Q = \frac{1}{2}(\|\Omega\|^2 - \|S\|^2), \tag{15}$$

where $\Omega_{ij} = \frac{1}{2}(\overline{U}_{i,j} - \overline{U}_{j,i})$ is the vorticity tensor and $S = \frac{1}{2}(\overline{U}_{i,j} + \overline{U}_{j,i})$ is the shear strain rate tensor and represents the symmetric and antisymmetric components of $\nabla\overline{\mathbf{U}}$, respectively.

Compared to the URANS results reported in Liu et al. (2022b), DDES reveals much more details of the turbulent structures. It can be clearly seen that the propeller wake flows at bollard condition for both the DP and RDT are very complex, with numerous turbulent small-scale coherent structures distributed along the streamwise direction in an irregular manner (as shown in Figs. 11(a) and 11(b)). This high turbulent nature of the wake has also been observed by Gaggero (2023), making it hard to identify a representative helical vortex system as defined for conventional open propellers. Therefore, to facilitate the interpretation of these vortical structures, the isosurface of Q-criterion with higer values are presented to visualize the stronger vortices, as shown in Figs. 11(b) and 11(d). For the DP, the complete helical filament of the tip vortex can be observed inside the duct with only a very limited distance before breakdown occurs when convected downstream. The short-wave instabilities, which are defined as the destabilization modes caused by the self-induced motion of a vortex filament with local deformation by Felli et al. (2011), can be detected as soon as the tip vortex is formed. This phenomenon is absent in case of the RDT due to the much weaker tip vortex as the propeller tip is sealed by the rim. In

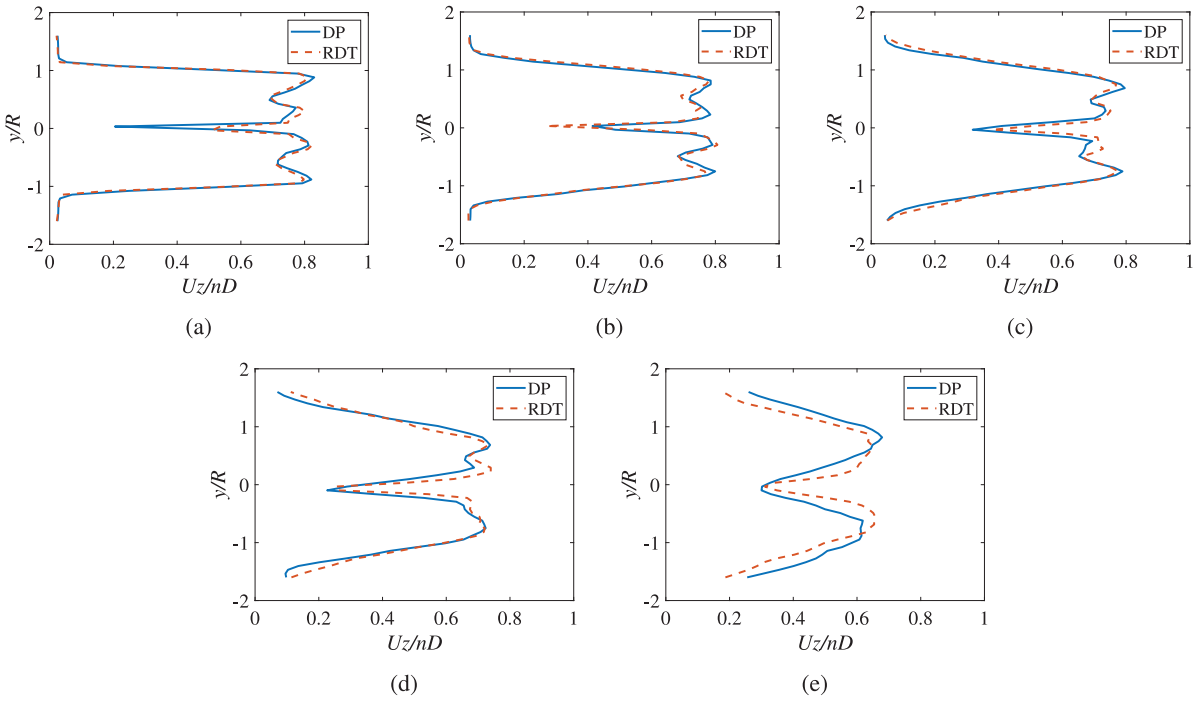

Fig. 6. Comparison of the axial velocity profiles at different locations in the wake between the DP and RDT; nD is the representative velocity of the propeller, which is 2 m/s in this case. (a) $z/R = 1$, (b) $z/R = 2$, (c) $z/R = 3$, (d) $z/R = 4$ and (e) $z/R = 6$.

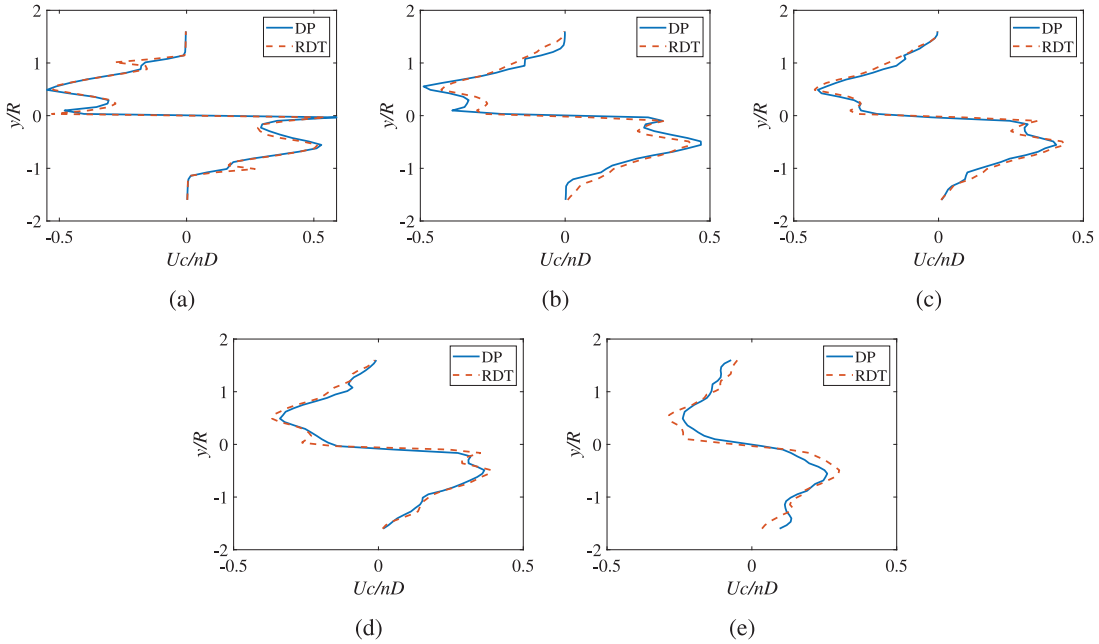

Fig. 7. Comparison of the circumferential velocity distribution at different locations in the wake between the DP and RDT; nD is the representative velocity of the propeller, which is 2 m/s in this case. (a) $z/R = 1$, (b) $z/R = 2$, (c) $z/R = 3$, (d) $z/R = 4$ and (e) $z/R = 6$.

the centre of the flow field, large coherent structures can be identified in both wakes, which are aligned with the flow direction. This system is called the hub vortex and is formed due to the bluff-body nature of the central hub. In case of the RDT, this hub vortex extends longer downstream before breaking up in small turbulent structures. Fig. 12 shows the distribution of the x-component of vorticity (out-of-plane component) in a longitudinal plane, which provides some insights into the interactions between vortices at different regions. The local velocity vectors at the tip region inside the duct, where the vortex core of the blade tip vortex exists, are also presented, indicating that the current mesh resolution is sufficient to capture the critical flow features. The interaction between the blade tip vortex and duct shear layer seems to be the most intensified, followed by the interactions between the blade trailing/root and hub vortices. For the DP, the inductance of the blade tip and duct appears to have a significant role in the destabilization of the hub vortex, resulting in a much earlier breakdown compared to the RDT. This could also be observed in Fig. 11, which shows the earlier brake up of the hub vortex for the DP.

In order to better understand the energy transfer mechanisms of the propeller wake during evolution, several probes are placed behind

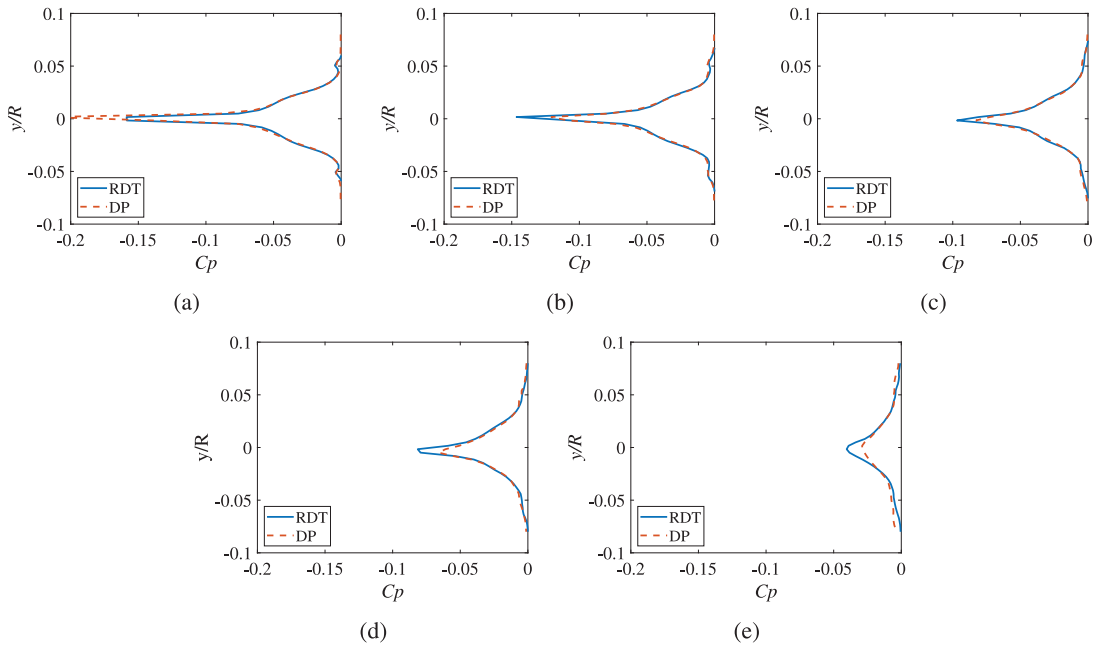

Fig. 8. Comparison of the pressure coefficient distribution at different axial locations in the wake between the DP and RDT. (a) $z/R = 1$, (b) $z/R = 2$, (c) $z/R = 3$, (d) $z/R = 4$ and (e) $z/R = 6$.

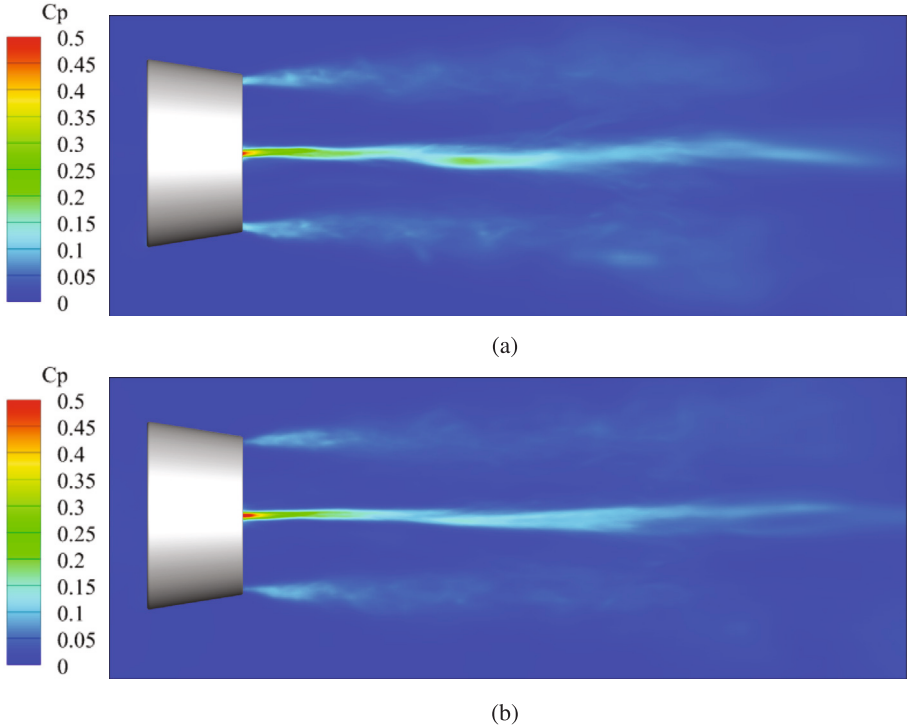

Fig. 9. Comparison of the root mean square pressure coefficient distribution in the wake between the DP and RDT: (a) DP and (b) RDT.

the propeller's tip and hub region for transient data collection. The probes are inserted in a yz-plane in a manner that may better capture the trajectory of the tip and hub vortex: fourteen probes are located at 0.5R, 1.0R, 1.5R, 2.5R, 3.5R, 4.5R and 5.5R at the tip region and three probes at 1.5R, 3.5R and 5.5R at the hub region, all along the streamwise direction, as suggested by Mascio et al. (2014) and Gong et al. (2018). Considering the contraction of the propeller wake, the first two probes (locations 1 and 2) in the tip region are at 0.95R in the radial direction, and all other locations are at similar axial positions at 0.90R. The diagram of probe positions in the wake of the DP and RDT is shown in Fig. 13. At each location, data are sampled during 13 rotations of the propeller with a sampling frequency of 100 kHz, giving a spectral resolution of 1.5 Hz and a minimum frequency of 1.5 Hz.

The spectra of the three velocity components for probe 1 are shown in Figure Fig. 14(a). A clear peak can be observed at 80 Hz, corresponding to four times the rotational speed of the propeller ($4n$). As the sampling location is close to the blade tip, the fluctuations are caused by the gap flow between the blades and the duct. The pressure

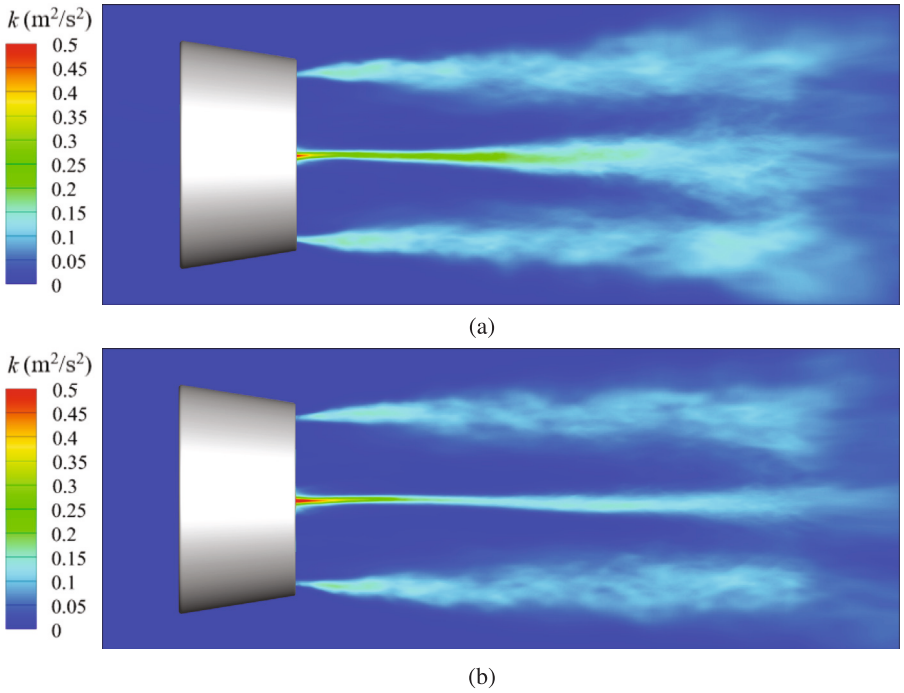

Fig. 10. Comparison of the kinetic energy distribution in the wake between the DP and RDT: (a) DP and (b) RDT.

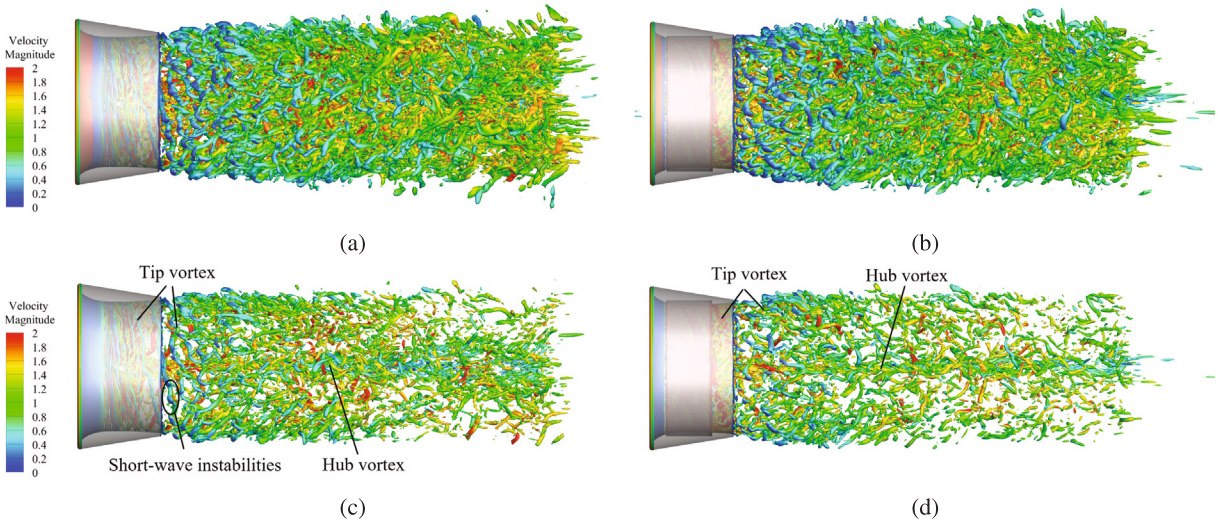

Fig. 11. The instantaneous structures in the wake of the DP (left) and RDT (right), with 3D vortical structures visualized using the Q-criterion.

spectrum (not shown here) reveals the same pronounced frequency peak at $4n$ (80 Hz). The rotational velocity component has the most pronounced peak, with a value of 9.5×10^{-3} followed by the radial velocity (8.7×10^{-3}) and the axial velocity (7.5×10^{-3}). The higher harmonics are also present in the spectra. Closer to the central axis at the same axial location (probe 11), the fluctuations are less pronounced (Fig. 14(b)). The major peak still appears at $4n$ (80 Hz) in the rotational velocity component, but the height (1.9×10^{-3}) is smaller compared to probe 1. Also in the pressure spectrum, the peak is reduced by about a factor 20. This is also depicted in the turbulence intensity in the rotational direction, $u_c'/\overline{U}_c$, which is about 50% for probe 1, while being 30% for probe 11. These observations indicate that the tip vortices behind the propeller blades are concentrated in a very narrow region near the blade tip, which was also visible in Figs. 11(a) and 11(c). Further downstream, in probe location 2 (Fig. 15(a)), the peak at $4n$ in the spectrum is more pronounced in the radial velocity component, instead of the rotational one. Moreover, multiple structures at low frequency appear in the spectrum of the axial velocity W in the range from $n/2$ to $2n$ (10–40 Hz). The pressure peak at probe 2 is also reduced by a factor of 2 compared to probe 1. Further downstream, the peak at $4n$ (80 Hz) gets less and less pronounced and several smaller peaks with low frequency content appear in the spectra. This is an indication that the tip vortices lose their coherence quite fast and break up in smaller turbulent structures. At the central axis in probe location 8 (Fig. 15(b)), no pronounced peak at $4n$ (80 Hz) can be found. Instead, several smaller peaks in the range between $n/4$ to $12n$ (5–240 Hz) are present, indicating the presence of several structures with different frequency content in the hub wake. These structures will be further analysed in the POD decomposition in the next section.

The frequency spectra of the RDT in the vicinity of the blades are shown in Fig. 16. Similar to the DP, probe 1 exhibits a clear peak at

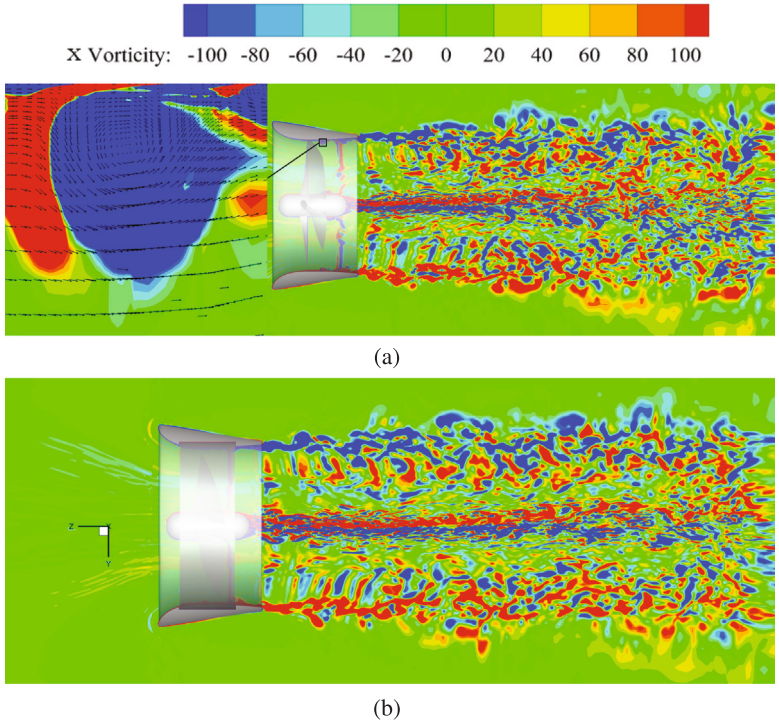

Fig. 12. Instantaneous x-vorticity distribution along the axial direction: (a) DP and (b) RDT.

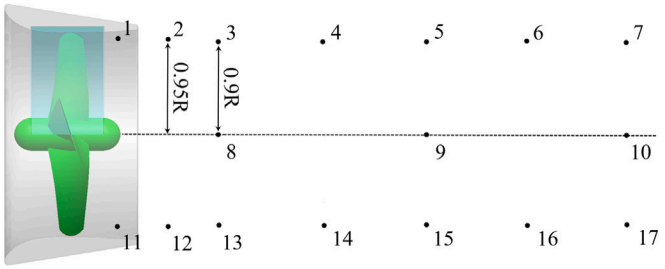

Fig. 13. Diagram of probing positions in the wake of the propellers.

$4n$ with a magnitude of 8.8×19^{-3} for the rotational velocity component. However, in contrast to the DP, the peak in the other velocity components is about 2 orders of magnitude smaller. This indicates that the blades of the RDT introduce mainly a rotational component in the flow field with negligible coherent fluctuations in the axial and radial direction. In case of the DP, these fluctuations are introduced by the tip vortices, which are not present in the RDT. In probe location 11 (Fig. 16(b)), the peak is significantly reduced for the rotational velocity component to 1.7×19^{-3}. The frequency peaks for the other velocity components are in the same order of magnitude. A little downstream, in probe location 2, the peaks at $4n$ and the associated harmonics are still present, together with the appearance of peaks at low frequencies, similar to the DP. At the central axis (probe 8, Fig. 17(b)), the frequency content is very similar to the DP (shown in Fig. 15(b)), indicating that the coherent structures in the hub vortex are very similar. It is worth noting that the pressure and velocity spectra of the DP in all different positions has exhibited higher peaks than those of the RDT, demonstrating that the RDT has a better performance in noise reduction. Further downstream of probe location 8, the peaks become very weak and barely visible as the spectra evolve towards the ones typically found in turbulent flow fields.

3.3. POD results

As can be seen from Fig. 11, the flow structures in both wakes are very complicated and large scale structures are masked by smaller turbulent ones. In order to be able to analyse these large structures, the flow field is decomposed using POD. As these structures often have a high energy content, they are contained in the lower modes if modes are ordered according to descending energy content. Data from three revolutions of the propeller are used as input. The energy content of the first 20 POD modes for both the DP and RDT is shown in Fig. 18. A significant difference can be observed in the energy distribution. For the DP, the energy is more distributed across the different modes, while for the RDT a significant peak is observed for mode 1. This mode is associated with the flow in the wake of the hub and has a very low frequency dynamic in the order of 60% of the rpm with no fixed frequency. This mode is not part of a rotating structure, unlike the modes following it. In the following discussion, the other modes are ordered according to descending energy content and the frequency peak of the associated temporal coefficient is mentioned in brackets in the caption. The first two modes of the DP and the RDT with the highest energy content (without mode 1 for the RDT as previously discussed) are shown in Fig. 19. The modes are visualized using iso-surfaces of static pressure. These iso-surfaces allow visualization of coherent structures behind the blades of the propeller, as well as the presence of vortex cores, which have a low pressure region in the centre (Jeong and Hussain, 1995; Percin et al., 2017). The first mode of the DP (Fig. 19(a)) represents the tip vortices in the gap flow behind the blades of the propeller and corresponding pressure fluctuations on the leading and trailing edges of the blades. The tip vortices are dissipated quite soon in the downstream direction as outside of the duct they are very weak. This was also confirmed by the analysis of the instantaneous vortical structures and the velocity spectra (Figs. 14(a) and 15(a)), where the peak at $4n$ decreases rapidly in the downstream direction. Mode one also displays structures in the wake behind the hub, which extend beyond $z/R = 4$ and are spirally winded around the central axis of the geometry. The dynamics of this structure can also be found in the spectra of probe 8, shown in Fig. 15(b). Mode one contains 10.6% of

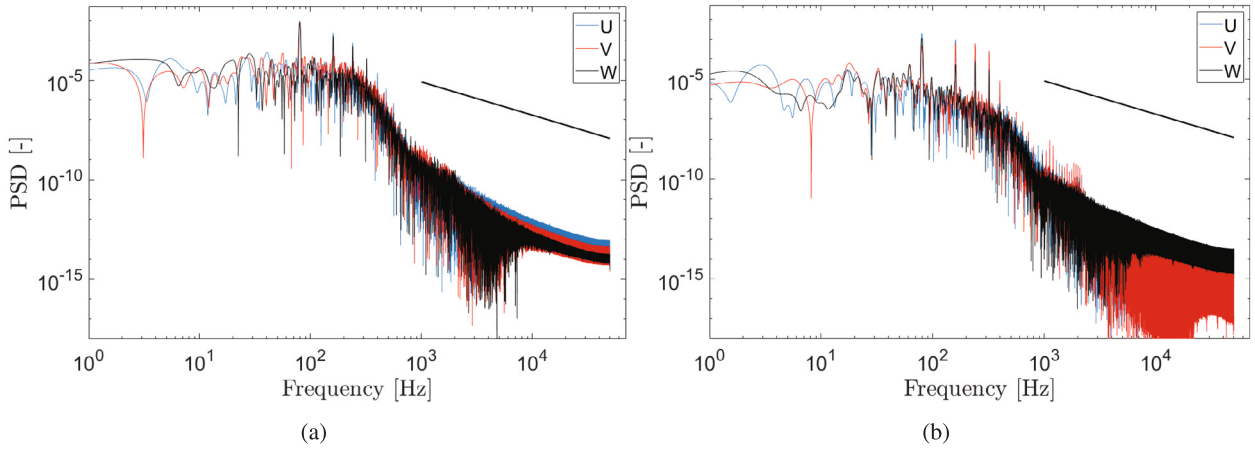

Fig. 14. Velocity spectra at probe locations 1 and 11 in the wake of the DP. The straight line indicates the −5/3 slope. (a) Probe 1 and (b) Probe 11.

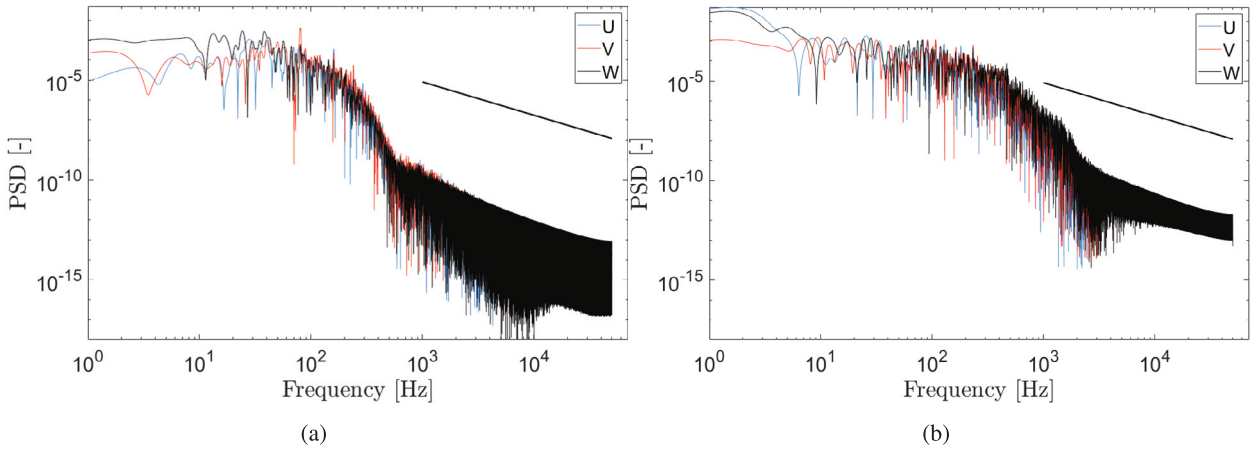

Fig. 15. Velocity spectra at probe locations 2 and 8 in the wake of the DP. The straight line indicates the −5/3 slope. (a) Probe 2 and (b) Probe 8.

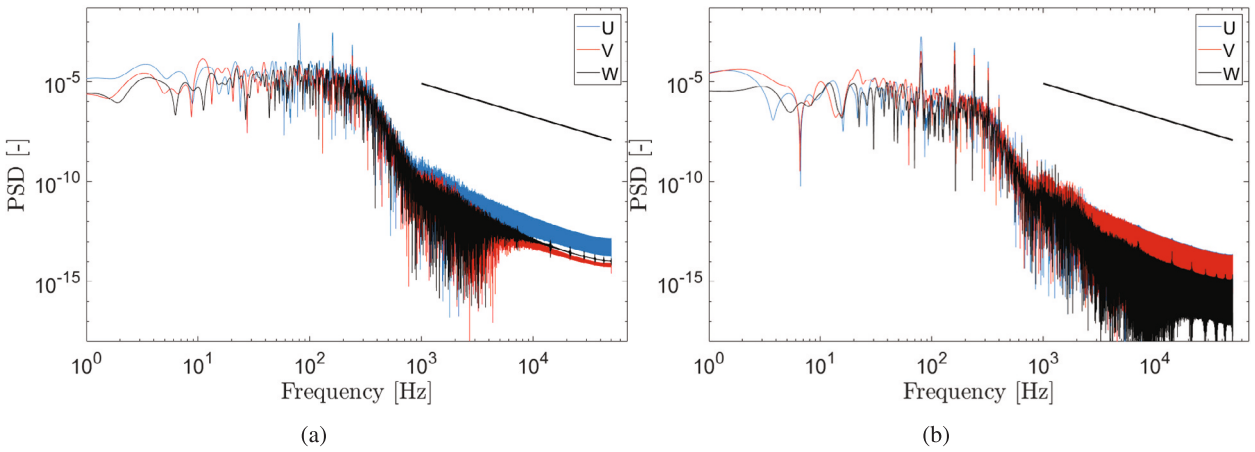

Fig. 16. Velocity spectra at probe locations 1 and 11 in the wake of the RDT. The straight line indicates the −5/3 slope. (a) Probe 1 and (b) Probe 11.

the total fluctuating energy in the wake flow of the DP and is hence a very pronounced structure. A spectral analysis of the time coefficient associated with mode one shows that the dominating frequency is 80 Hz, equal to $4n$. Hence mode 1 is responsible for the pronounced peaks in probe locations 1 and 2. The second most energetic mode in the wake of the DP, shown in Fig. 19(c), has exactly the same spatial structure as the first mode and is rotated around the central axis with an angle of $\pi/8$ with respect to mode one. The corresponding temporal coefficient is also shifted by $\pi/2$ which means that both modes are orthogonal components of a rotating structure representing the near field fluctuations caused by the tip vortices in the gap flow of the rotating blades.

The two most energetic modes in the RDT wake are shown in Figs. 19(b) and 19(d). These modes represent a helical structure formed in the wake of the hub and hence represent the hub vortex. This spiralling structure forms due to the bluff-body nature of the hub and similar structures have previously been reported in other rotating bluff body flows, such as the annular swirling jet (Zhang and Vanierschot,

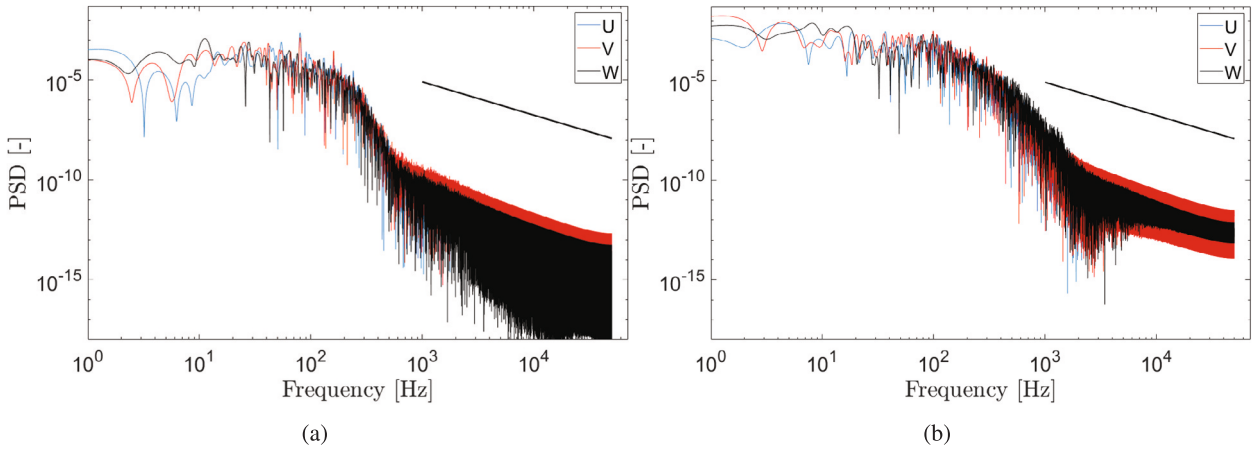

Fig. 17. Velocity spectra at probe locations 2 and 8 in the wake of the RDT. The straight line indicates the −5/3 slope. (a) Probe 2 and (b) Probe 8.

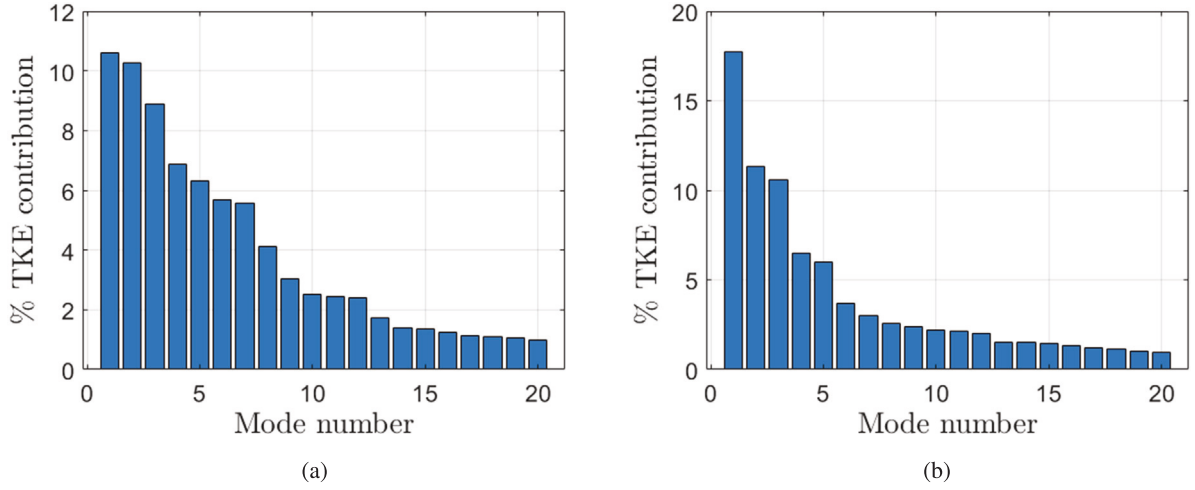

Fig. 18. Energy content of the 20 most energetic POD modes. (a) DP and (b) RDT.

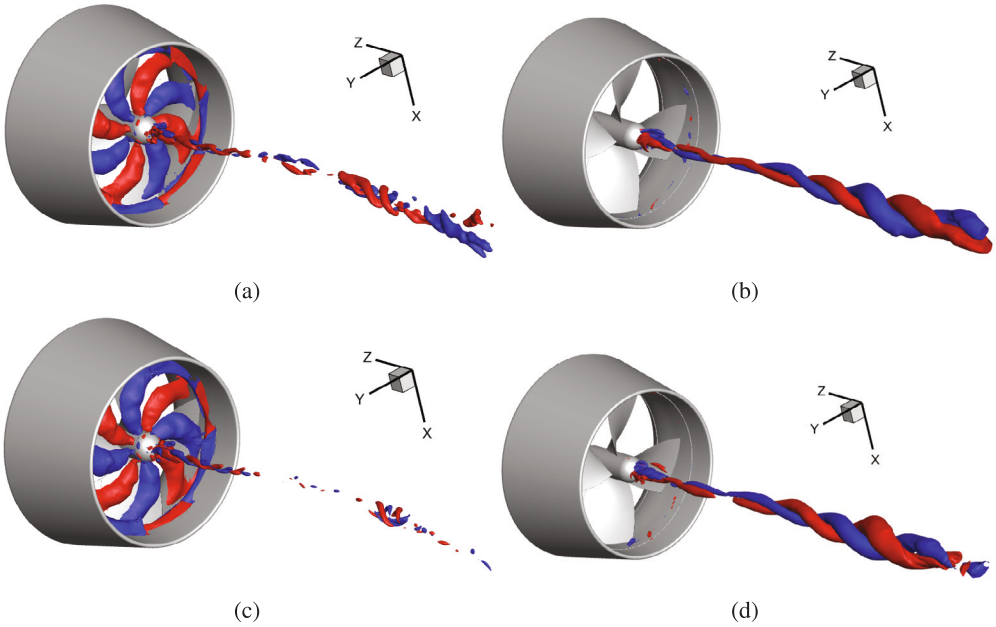

Fig. 19. First 2 POD modes with the highest energy content and the corresponding temporal dynamics of the associated time coefficient. The red isosurfaces are values of $P = -1$ Pa and the blue isosurfaces of $P = 1$ Pa. Left, the structures in the DP wake and right, the ones in the RDT wake. (a) First mode with 10.6% energy content ($4n$), (b) First mode with 11.3% energy content (n), (c) Second mode with 10.3% energy content ($4n$) and (d) Second mode with 10.6% energy content (n).

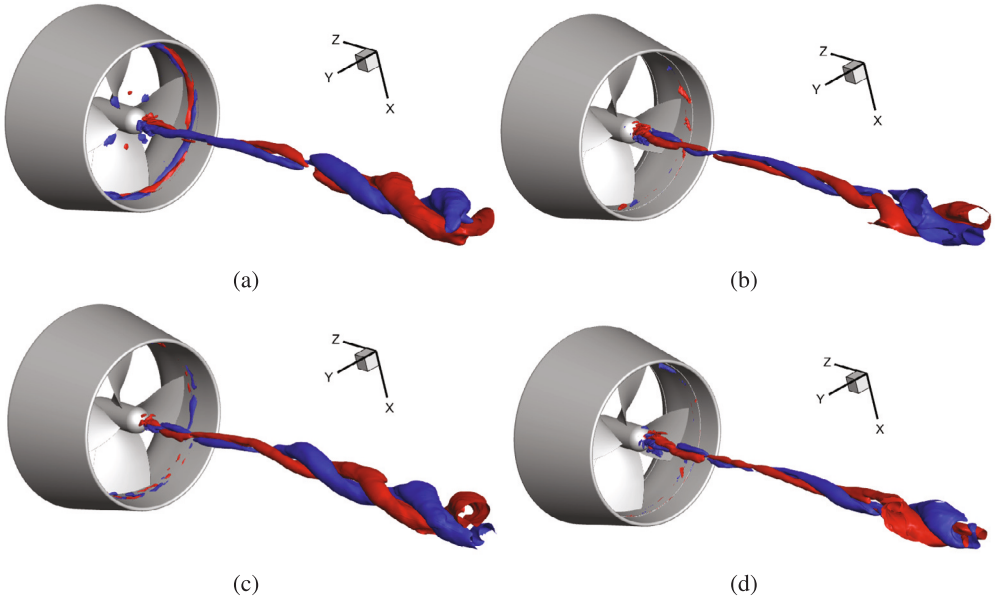

Fig. 20. POD modes with the highest energy content and the corresponding temporal dynamics of the associated time coefficient. The red isosurfaces are values of $P = -1$ Pa and the blue isosurfaces of $P = 1$ Pa. Left, the structures in the DP wake and right, the ones in the RDT wake. (a) Third mode with 8.9% energy content ($n/1.5$), (b) Third mode with 6.5% energy content ($n/2$), (c) Fourth mode with 6.9% energy content ($n/1.5$) and (d) Fourth mode with 6.0% energy content ($n/2$).

2021a; Percin et al., 2017; Vanierschot and Ogus, 2019; Vanierschot et al., 2020; Zhang and Vanierschot, 2021b). The associated time coefficients show a distinct peak at the rotational speed of the propeller. Both spatial modes are rotated $\pi/2$ around the central axis of the geometry and the associated time coefficients also have a phase shift of $\pi/2$. Hence both modes represent a single spiral helix rotating around the central axis of the RDT at a rotational speed n.

The same spiralling structure in the centre of the RDT wake is also represented by modes three and four (Figs. 20(b) and 20(d)). The frequency is half of the rpm ($n/2$), while the pitch of the spiral is double compared to the structures in Figs. 19(b) and 19(d). Nevertheless, from the Lissajous figures of the temporal coefficients (not shown here), it was not clear whether both are harmonics of each other or not. In the wake of the DP, a similar central spiralling structure is also present, represented by modes three and four (Figs. 20(a) and 20(c)). The temporal coefficients of both structures have a main frequency peak at $n/1.5$, but the temporal coefficient of mode three also contains a peak at $4n$, corresponding to the tip vortices of the propeller blades. These structures are also identified in Fig. 20(a). Hence POD is not able to fully separate structures into individual modes as these structures might be present in several other modes. Similar studies have also observed this for other rotating bluff body flows, like the annular swirling jet (Vanierschot et al., 2020; Zhang and Vanierschot, 2021b). Due to the presence of the tip vortices, the energy content of mode three is also slightly larger than the energy content of mode four.

The fifth mode in the wake of the DP is shown in Fig. 21(a). It is a very slowly rotating structure with a long pitch. The main peak in the spectrum of the temporal coefficient is at $n/3$, while there is also a peak present at $8n$, related to the presence of tip vortices in the mode. However, in contrast to several other spiralling structures found in the wake, this mode does not have a pronounced similar orthogonal mode representing a precessing pair. The sixth mode in the wake of the DP is shown in Fig. 21(c). This mode represents the tip vortices at the gap flow and has a frequency peak at $8n$. This is exactly double the one of modes one and two and the Lissajous figures of the temporal coefficients (not shown here) confirm that mode six is the second harmonic of modes one and two. The other mode of the precessing pair is shown in Fig. 22(a). The fifth and sixth mode in the wake of the RDT represent another spiralling structure around the central axis of the propeller, which has a peak in the frequency spectra at $n/1.2$.

The seventh and eighth mode pair in the wake of the RDT are shown in Figs. 22(b) and 22(d). These modes represent the pressure fluctuations due to the rotating blades and are also found in the DP in modes one and two (Figs. 19(a) and 19(c)). The energy content is much smaller than the structures in the DP wake. The modes also represent a double helical structure near the central axis, which was not present in the DP wake. The last POD mode in the wake of the DP is shown in Fig. 22(c). This spiralling structure rotates at $n/2$ and is similar to the one in the wake of the RDT in modes five and six (Figs. 21(b) and 21(d)). The above analysis shows that for both the DP and RDT, the 8 POD modes with highest energy content focus on either the near field region of the blades and the tip vortices (most dominant in the DP wake) or on the central region of the hub vortex (most dominant for the RDT. The former one consists of different spiralling structures with a wide variety of frequencies and pitches, explaining the low frequency peaks found in the spectra of probe locations 8, 9 and 10 in Fig. 13.

4. Conclusion

The wake dynamics of a propeller is highly important for its performance prediction as it provides valuable insights into the formation and evolution of complex vortical structures in the flow field. The present work investigates the wake topology of a rim-driven thruster (RDT) and a ducted propeller (DP) with the same design and geometrical size. Delayed Detached Eddy Simulations (DDES) along with the sliding mesh technique are employed to resolve the flow field around the propeller. The bollard condition is studied in this work as in this condition, the propeller loading is the heaviest and it can therefore trigger the most complex vortical structures, hence generating the most intense noise. Proper orthogonal decomposition is also adopted to further analyse the coherent structures which contain the most kinetic energy. Based on the simulation results, some findings are summarized below:

- From the statistical results it is observed that the axial velocity profiles in the wake of both the DP and RDT exhibit a similar pattern, with two shear layers present in the wake and the velocity deficit caused by positive pressure gradients is higher for the DP than for the RDT.

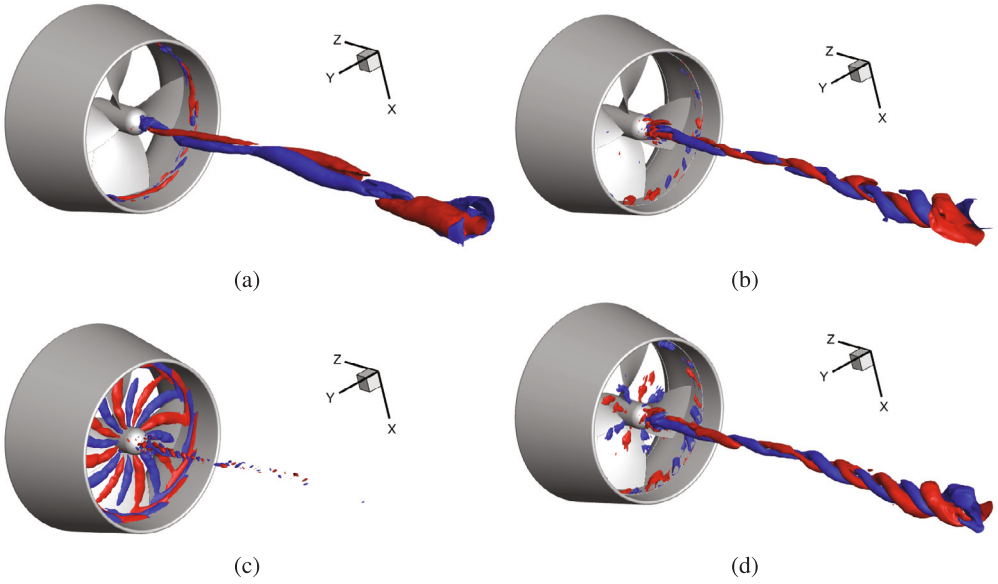

Fig. 21. POD modes with the highest energy content and the corresponding temporal dynamics of the associated time coefficient. The red isosurfaces are values of $P = -1$ Pa and the blue isosurfaces of $P = 1$ Pa. Left, the structures in the DP wake and right, the ones in the RDT wake. (a) Fifth mode with 6.3% energy content ($n/3$), (b) Fifth mode with 3.7% energy content ($n/1.2$), (c) Sixth mode with 5.7% energy content ($8n$) and (d) Sixth mode with 3.0% energy content ($n/1.2$).

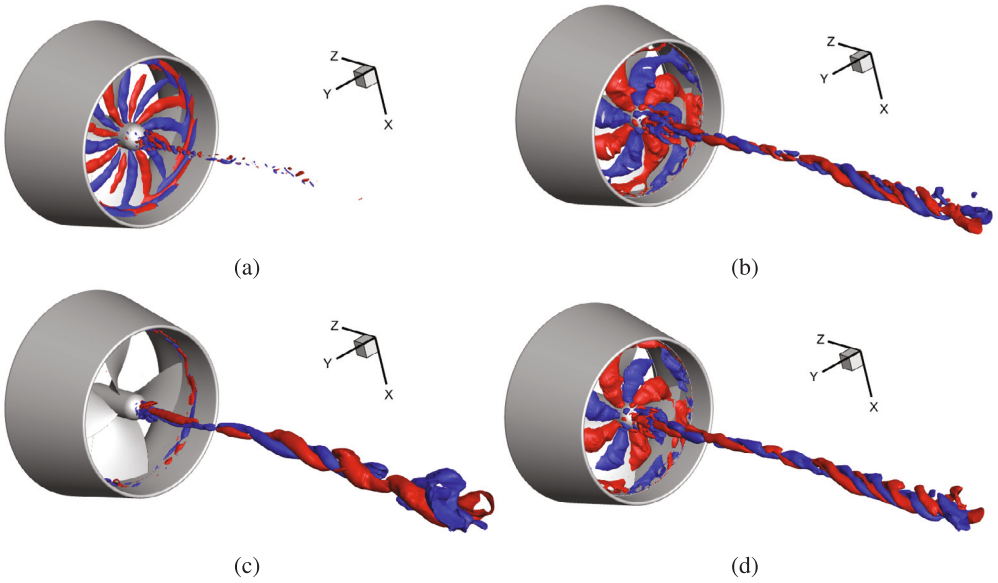

Fig. 22. POD modes with the highest energy content and the corresponding temporal dynamics of the associated time coefficient. The red isosurfaces are values of $P = -1$ Pa and the blue isosurfaces of $P = 1$ Pa. Left, the structures in the DP wake and right, the ones in the RDT wake. (a) Seventh mode with 5.6% energy content ($8n$), (b) Seventh mode with 2.6% energy content ($4n$), (c) Eighth mode with 4.1% energy content ($n/1.2$) and (d) Eighth mode with 2.4% energy content ($4n$).

- For the DP, the tip leakage flow intensifies the interactions between the blade tip and duct, resulting in a higher fluctuating component of pressure compared to the RDT. The instantaneous flow fields which are visualized with 3D vortical structures demonstrate complicated composition and evolution of vortical systems for both the DP and RDT.
- The complete helical filament of the blade tip vortex is visible in the DP but travels only a limited distance downstream before breaking up, while it is totally absent in the case of the RDT as there is no tip clearance and therefore the tip vortex is significantly reduced.
- The POD analysis shows that for both the DP and RDT, the 8 POD modes with highest energy content focus on either the near field region of the blades and the tip vortices (most dominant in the DP wake) or on the central region of the hub vortex (most dominant for the RDT wake).
- The former one consists of different spiralling structures with a wide variety of frequencies and pitches, explaining the low frequency peaks found in the spectra of probe locations on the central axis of the wake.

The methods and results presented in this work can provide some insights into the wake dynamics of a rim-driven thruster, which is considered to be an important perspective of evaluation of the RDT performance.

CRediT authorship contribution statement

Bao Liu: Writing – original draft, Investigation, Formal analysis, Data curation, Conceptualization. **Xinping Yan:** Writing – review &

editing, Supervision, Funding acquisition. **Wu Ouyang:** Writing – review & editing, Supervision, Project administration, Funding acquisition. **Maarten Vanierschot:** Writing – review & editing, Writing – original draft, Supervision, Software, Methodology, Conceptualization.

Declaration of competing interest

The authors declare that they have no known competing financial interests or personal relationships that could have appeared to influence the work reported in this paper.

Data availability

Data will be made available on request.

Acknowledgements

This project was financially supported by the National Key Research and Development Program of China (No. 2022YFB4300802) and the Fundamental Research Funds for the Central Universities (WUT:2023IVA084). The computational resources and services used in this work were provided by the VSC (Flemish Supercomputer Center), funded by the Research Foundation - Flanders (FWO) and the Flemish Government – department EWI.

References

Baek, D., Yoon, H., Jung, J., Kim, K., Paik, B., 2015. Effects of the advance ratio on the evolution of a propeller wake. Comput. Fluids. 118, 32–43.
Dubas, A., Bressloff, N., Sharkh, S., 2015. Numerical modelling of rotor–stator interaction in rim driven thrusters. Ocean Eng. 106, 281–288.
Felli, M., Camussi, R., Di Felice, F., 2011. Mechanisms of evolution of the propeller wake in the transition and far fields. Exp. Fluids 682, 5–53.
Felli, M., Falchi, M., 2018. Propeller wake evolution mechanisms in oblique flow conditions. J. Fluid Mech. 845, 520–559.
Gaggero, S., 2020. Numerical design of a rim-driven thruster using a RANS-based optimization approach. Appl. Ocean Res. 94, 101941.
Gaggero, S., 2023. A study on the wake evolution of a set of rim-driven thrusters. J. Mar. Sci. Eng. 11.
Gong, J., Ding, J., Wang, L., 2021. Propeller–duct interaction on the wake dynamics of a ducted propeller. Phys. Fluids 33, 074102.
Gong, J., Guo, C., Zhao, D., Wu, T., Song, K., 2018. A comparative DES study of wake vortex evolution for ducted and non-ducted propellers. Ocean Eng. 160, 78–93.
Guo, C., Yang, C., Sun, C., Wang, C., Yao, H., Lin, J., 2023. Influence of jet flow on hydrodynamic performance of a ducted propeller. Phys. Fluids 35, 125120.
Jeong, J., Hussain, F., 1995. On the identification of a vortex. J. Fluid Mech. 285, 69–94.
Jiang, Y., Li, Y., Wu, C., Qing, W., Zhang, G., 2021. Assessment of RANS and DES turbulence models for the underwater vehicle wake flow field and propeller excitation force. J. Mar. Sci. Technol. 27.
Li, P., Sun, C., Yao, H., Wang, Z., Wang, C., Weng, K., 2023a. The effects of domain division types on the performance prediction of a rim-driven thruster. Ocean Eng. 287, 115809.
Li, P., Yao, H., Wang, C., Weng, K., 2023b. Improved efficiency with concave cavities on S3 surface of a rim-driven thruster. Phys. Fluids 35 (10), 107102.
Liu, B., Dai, M., Liang, X., 2023c. Influence of bearings on the open water performance of a rim-driven thruster. Phys. Fluids 138, 085139.
Liu, B., Vanierschot, M., 2021. Numerical study of the hydrodynamic characteristics comparison between a ducted propeller and a rim-driven thruster. Appl. Sci. Basel. 11, 4919.
Liu, B., Vanierschot, M., Buysschaert, F., 2022a. Effects of transition turbulence modeling on the hydrodynamic performance prediction of a rim-driven thruster under different duct designs. Ocean Eng. 256, 111142.
Liu, B., Vanierschot, M., Buysschaert, F., 2022b. Study of wake dynamics of a rim-driven thruster based on numerical methods. In: Proceedings of the International Conference on Computational Fluid Dynamics in Civil Engineering. Bali, Indonesia.
Liu, B., Vanierschot, M., Buysschaert, F., 2023b. Optimization design of the duct of a rim-driven thruster using the adjoint approach. Ocean Eng. 278, 114293.
Lungu, A., 2020. A DES-SST based assessment of hydrodynamic performances of the wetted and cavitating PPTC propeller. J. Mar. Sci. Eng. 8 (4), 297.
Lungu, A., 2022. A DES-based study of the flow around the self-propelled DARPA suboff working in deep immersion and beneath the free-surface. Ocean Eng. 244, 110358.
Mahesh, K., Kumar, P., Gnanaskandan, A., Nitzkorski, Z., 2015. LES applied to ship research. J. Ship Res. 59, 238–245.
Mascio, A., Muscari, R., Dubbioso, G., 2014. On the wake dynamics of a propeller operating in drift. J. Fliud Mech. 754.
Menter, F., 1994. Two-equation eddy-viscosity turbulence models for engineering applications. AIAA J. 32, 1598–1605.
Nie, Y., Ouyang, W., Zhang, Z., Li, G., Zheng, R., 2023. Multi-parameter optimization analysis of hydrodynamic performance for rim-driven thruster. Energies. 16.
Oosterveld, M.W.C., 1970. Wake adapted ducted propellers. No. NSMB-345.
Percin, M., Vanierschot, M., van Oudheusden, B., 2017. Analysis of the pressure fields in a swirling annular jet flow. Exp. Fluids 58 (12), 166.
Posa, A., Felli, M., Broglia, R., 2023. Acoustic far field of a propeller working in the wake of a hydrofoil. Phys. Fluids 35, 125121.
Song, B., Wang, Y., Tian, W., 2015. Open water performance comparison between hub-type and hubless rim driven thrusters based on CFD method. Ocean Eng. 103, 55–63.
Vanierschot, M., Müller, J.S., Sieber, M., Percin, M., van Oudheusden, B.W., Oberleithner, K., 2020. Single- and double-helix vortex breakdown as two dominant global modes in turbulent swirling jet flow. J. Fluid Mech. 883, A31.
Vanierschot, M., Ogus, G., 2019. Experimental investigation of the precessing vortex core in annular swirling jet flows in the transitional regime. Exp. Therm Fluid Sci. 106, 148–158.
Viitanen, V., Hynninen, A., Sipilä, T., Siikonen, T., 2018. DDES of wetted and cavitating marine propeller for CHA underwater noise assessment. J. Mar. Sci. Eng. 6, 56.
Wang, L., Guo, C., Su, Y., Wu, T., 2018. A numerical study on the correlation between the evolution of propeller trailing vortex wake and skew of propellers. Int. J. Nav. Archit. Ocean Eng. 10, 212–224.
Wang, L., Guo, C., Xu, P., Su, Y., 2019. Analysis of the wake dynamics of a propeller operating before a rudder. Ocean Eng. 188, 106250.
Wang, L., Liu, X., Chao, X., Guo, J., Liao, J., 2023. Modeling of wake features of a propeller using the vorticity confinement method. Phys. Fluids 35, 075134.
Wang, L., Wu, T., Gong, J., Yang, Y., 2021. Numerical analysis of the wake dynamics of a propeller. Phys. Fluids 33, 095120.
Witte, M., Hieke, M., Wurm, F.-H., 2019. Identification of coherent flow structures and experimental analysis of the hydroacoustic emission of a hubless propeller. Ocean Eng. 188, 106248.
Yakovlev, A., Sokolov, M., Marinich, N., 2011. Numerical design and experimental verification of a rim-driven thruster. In: Proceedings of 2nd International Symposium on Marine Propulsors. pp. 396–403.
Yan, X., Liang, X., Ouyang, W., Liu, Z., Liu, B., Lan, J., 2017. A review of progress and applications of ship shaft-less rim-driven thrusters. Ocean Eng. 144, 142–156.
Yang, C., Sun, C., Wang, C., Yao, H., Guo, C., Yue, Q., 2024. Serration of the duct trailing edge to affect the hydrodynamics and noise generation for a pump-jet propulsor. Phys. Fluids 36 (1), 015140.
Yu, C., Wang, R., Zhang, X., Li, Y., 2020. Experimental and numerical study on underwater radiated noise of AUV. Ocean Eng. 201, 107111.
Zhai, S., Jin, S., Chen, J., Liu, Z., Song, X., 2022. CFD-based multi-objective optimization of the duct for a rim-driven thruster. Ocean Eng. 264.
Zhang, Q., Jaiman, R., 2019. Numerical analysis on the wake dynamics of a ducted propeller. Ocean Eng. 171, 202–224.
Zhang, X., Liu, Z., Cao, L., Wan, D., 2022. Tip clearance effect on the tip leakage vortex evolution and wake instability of a ducted propeller. J. Mar. Sci. Eng. 10, 1007.
Zhang, Y., Vanierschot, M., 2021a. Determination of single and double helical structures in a swirling jet by spectral proper orthogonal decomposition. Phys. Fluids 33 (1), 015115.
Zhang, Y., Vanierschot, M., 2021b. Modeling capabilities of unsteady RANS for the simulation of turbulent swirling flow in an annular bluff-body combustor geometry. Appl. Math. Model. 89, 1140–1154.
Zhao, X., Shen, X., Geng, L., Zhang, D., van Esch, B., 2023. Comparative study on the wake dynamics of pump-jet and ducted propeller based on dynamic mode decomposition. Phys. Fluids 35, 115135.
Zhu, W., Gao, H., 2019. A numerical investigation of a winglet-propeller using an LES model. J. Mar. Sci. Eng. 7, 333.